

**1 Climatology, seasonality, and trends of oceanic coherent
2 eddies**

3 Josué Martínez-Moreno¹, Andrew McC. Hogg¹, and Matthew H. England²

4 ¹Research School of Earth Science and ARC Center of Excellence for Climate Extremes, Australian
5 National University, Canberra, Australia

6 ²Climate Change Research Centre (CCRC), UNSW Australia, Sydney NSW, Australia

7 Key Points:

- 8 • Kinetic energy of coherent eddies contain around 50% of the surface ocean kinetic
9 energy budget.**
- 10 • Seasonal cycle of the number of coherent eddies and coherent eddy amplitude re-
11 veal a 3-6 month lag to wind forcing**
- 12 • Inverse cascade sets up the seasonal lag of the number and amplitude of coher-
13 ent eddies.**
- 14 • The coherent eddy amplitude has increase at a rate of 3 cm per decade since 1993.**

Corresponding author: Josué Martínez-Moreno, josue.martinezmoreno@anu.edu.au

15 **Abstract**

Ocean eddies influence regional and global climate through mixing and transport of heat and properties. One of the most recognizable and ubiquitous feature of oceanic eddies are vortices with spatial scales of tens to hundreds of kilometers, frequently referred as “mesoscale eddies” or “coherent eddies”. Coherent eddies are known to transport properties across the ocean and to locally affect near-surface wind, cloud properties and rainfall patterns. Although coherent eddies are ubiquitous, yet their climatology, seasonality and long-term temporal evolution remains poorly understood. Thus, we examine the kinetic energy contained by coherent eddies and we present the annual and long-term changes of automatically identified coherent eddies from satellite observations from 1993 to 2019. Around 50% of the kinetic energy contained by ocean eddies corresponds to coherent eddies. Additionally, a strong hemispherical seasonal cycle is observed, with a 3–6 months lag between the wind forcing and the response of the coherent eddy field. Furthermore, the seasonality of the number of coherent eddies and their amplitude reveals that the number of coherent eddies responds faster to the forcing (~ 3 months), than the coherent eddy amplitude (which is lagged by ~ 6 months). Our analysis highlights the relative importance of the coherent eddy field in the ocean kinetic energy budget, implies a strong response of the eddy number and eddy amplitude to forcing at different time-scales, and showcases the seasonality, and multidecadal trends of coherent eddy properties.

35 **Plain language summary**36 **1 Introduction**

Mesoscale ocean variability with spatial scales of tens to hundreds of kilometers is comprised of processes such as vortices, waves, and jets (Ferrari & Wunsch, 2009; Fu et al., 2010). These mesoscale processes are highly energetic, and they play a crucial role in the transport of heat, salt, momentum, and other tracers through the ocean (Wunsch & Ferrari, 2004; Wyrtki et al., 1976; Gill et al., 1974). Possibly, the most recognizable and abundant process observed from satellites is mesoscale vortices. Although mesoscale vortices are commonly referred to in literature as “mesoscale eddies”, this term is also often used to describe the total mesoscale ocean variability (the time-varying component of the mesoscale flow), thus, here we will refer to mesoscale vortices as *coherent eddies*.

46 Coherent eddies are quasi-circular currents. According to their rotational direction,
47 the sea surface height anomaly within a coherent eddy can have a negative or positive
48 sea surface height anomaly (cold-core and warm-core coherent eddies, respectively). This
49 characteristic sea surface height signature of coherent eddies has been utilized to auto-
50 matically identify and track coherent eddies from satellite altimetry (Cui et al., 2020;
51 Martínez-Moreno et al., 2019; Ashkezari et al., 2016; Faghmous et al., 2015; Chelton et
52 al., 2007). Automated identification algorithms of coherent eddies have shown their ubiq-
53 uituity in the oceans, with a predominant influence at hotspots of eddy activity such as bound-
54 ary extensions and the Antarctic Circumpolar Current. In these regions, Chelton et al.
55 (2011) estimated that coherent eddies contribute around 40–50% of the mesoscale kinetic
56 energy (Chelton et al., 2011) and thus a significant fraction of the total kinetic energy
57 (Ferrari & Wunsch, 2009). Although this unique estimate showcases the importance of
58 the mesoscale coherent eddy field, the energy contained by coherent eddies was estimated
59 by extracting the geostrophic velocities within the detected coherent eddies, thus it is
60 possible it may contain energy from other processes. Coherent eddies are not only abun-
61 dant and may have a large proportion of the surface kinetic energy budget, but they are
62 also essential to ocean dynamics as concluded by many previous studies (Patel et al., 2020;
63 Schubert et al., 2019; Pilo et al., 2015; Frenger et al., 2015, 2013; Beron-Vera et al., 2013;
64 Siegel et al., 2011; Hogg & Blundell, 2006).

65 There is broad consensus that mesoscale eddy kinetic energy has a pronounced sea-
66 sonal variability (Uchida et al., 2017; Kang & Curchitser, 2017; Qiu & Chen, 2004; Qiu,
67 1999). Several hypotheses have been proposed to explain this seasonality including: sea-
68 sonal variations of atmospheric forcing (Sasaki et al., 2014), seasonality of the mixed layer
69 depth (Qiu et al., 2014; Callies et al., 2015), seasonality of the intensity of barotropic in-
70 stability (Qiu & Chen, 2004), the variability of the baroclinic instability due to the sea-
71 sonality of the vertical shear (Qiu, 1999), and a seasonal lag of the inverse energy cas-
72 cade (i.e. energy is transported between scales, from small to large; Arbic et al., 2013)
73 in combination with the presence of a front in the mixed layer, which can lead to a sea-
74 sonal cycle of the baroclinic instability (Qiu et al., 2014). On one hand, processes such
75 as barotropic and baroclinic instabilities control the seasonality of coherent eddies in the
76 ocean. On the other hand, recent studies using observations and eddy-permitting climate
77 models suggest several long-term adjustments of the global ocean capable of long-term
78 changes in the coherent eddy field. Such readjustments include a multidecadal increase

in the ocean stratification resulted from temperature and salinity changes (Li et al., 2020), a horizontal readjustment of the sea surface temperature gradients (Ruela et al., 2020; Bouali et al., 2017; Cane et al., 1997), and an intensification of the kinetic energy, eddy kinetic energy, and mesoscale eddy kinetic energy over the last 3 decades as a consequence of an increase in wind forcing (Hu et al., 2020; Wunsch, 2020; Martínez-Moreno et al., 2021). All these seasonal factors and long-term readjustments directly influence the annual and decadal response of the coherent eddy field, however, the seasonality of the coherent component of the eddy kinetic energy, as well as the seasonal cycle and trends of the coherent eddy statistics remain unknown.

Here we present a new global climatology of the coherent eddy kinetic energy by reconstructing the coherent eddy signature from satellite observations. Our study documents the seasonal cycle of the coherent eddy kinetic energy, and seasonal cycle and long-term trends of the coherent eddy properties over the satellite record. Moreover, we conduct more detail analysis in regions where coherent eddies dominate the eddy kinetic energy field. This paper is structured as follows: the data sources and methodology are described in section 2. Then, we present the climatology, energy ratios, and global seasonality of the coherent eddy kinetic energy in section 3. Section 4 presents the global climatology and seasonality of coherent eddy properties, followed by long-term changes of the coherent eddy properties (section 5). Then we focus our attention on the seasonal cycle and coherent eddy properties in regions dominated by coherent eddies (section 6). Finally, section 7 summarizes the main results and discusses the implications of this study.

2 Methods

We use daily sea surface height (SSH) data made available by the Copernicus Marine Environment Monitoring Service in near real time (CMEMS, 2017). This gridded product contains the sea surface height and geostrophic velocities with daily 0.25° resolution from January 1993 to 2019. The daily geostrophic velocities allowed us to compute the kinetic energy (KE) and eddy kinetic energy (EKE) over the satellite record. The main source of EKE is the time-varying wind (Ferrari & Wunsch, 2009), thus we computed the seasonal cycle of the wind magnitude from the JRA55 reanalysis (Japan Meteorological Agency, Japan, 2013) using wind velocities at 10m above the ocean's surface.

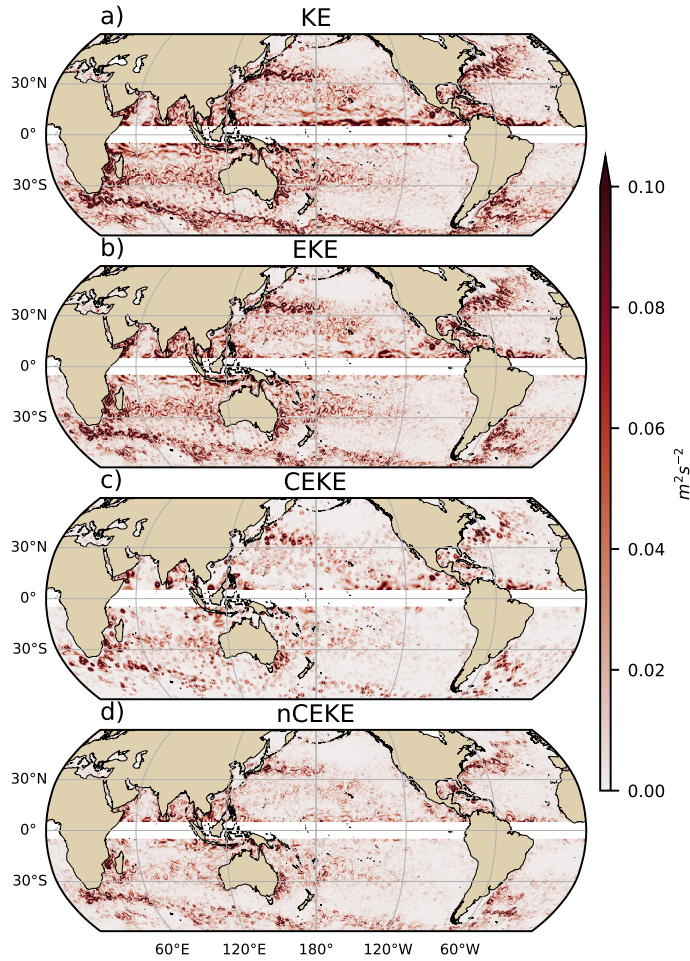
Over the same record, coherent eddy statistics from Martínez-Moreno et al. (2019), hereafter M-M, are analyzed and compared to those released by Chelton & Schlax (2013), both datasets are gridded in a 1° resolution. Although both datasets are produced via automated eddy identification algorithms using closed contours of SSH, these datasets have important differences in the criteria they use to identify and record coherent eddies statistics. The major differences include; (i) M-M's algorithm requires an adjustment between a 2D Gaussian and the SSH anomaly (SSHa) surface within the identify closed contour, while Chelton's only uses the outer-most closed contour of SSH; (ii) M-M's dataset reports the maximum SSHa within the identified coherent eddy, while Chelton's algorithm reports the maximum SSH value minus the discrete level in which the coherent eddy was identified; M-M's dataset includes all detected coherent eddies, while Chelton's dataset excludes (iii) coherent eddies with lifetimes shorter than four weeks and (iv) coherent eddy amplitudes smaller than 1cm. Moreover, M-M's algorithm allows the reconstruction of the coherent eddy field under the assumption that coherent eddies have a 2D Gaussian imprint in the sea surface height. This Gaussian reconstruction of the coherent eddy field then allow us to estimate the coherent geostrophic eddy velocities and thus the kinetic energy contained only by coherent eddies.

2.1 Kinetic Energy decomposition

Kinetic energy is commonly divided into the mean and time-varying components through a Reynolds decomposition. At a given time, the surface velocity field $\mathbf{u} = (u, v)$ is split into the time mean ($\bar{\mathbf{u}}$) and time varying components (\mathbf{u}'). Moreover, M-M proposed to further decompose the eddy kinetic energy into the energy contained by coherent features (\mathbf{u}'_e) and non-coherent features (\mathbf{u}'_n). Therefore the KE equation can be written as:

$$\text{KE} = \underbrace{\bar{u}^2 + \bar{v}^2}_{\text{MKE}} + \underbrace{u'^2_e + v'^2_e + u'^2_n + v'^2_n}_{\text{CEKE}} + \underbrace{\mathcal{O}_c^2}_{\text{nCEKE}} + \mathcal{O}^2 \quad (1)$$

Due to the properties of this decomposition, the second order term \mathcal{O}^2 is zero when averaged over the same period as $\bar{\mathbf{u}}$. However, \mathcal{O}_c^2 is not necessarily negligible, unless it is averaged over time and space. More information about the decomposition of the field into coherent features and non-coherent features is explained by Martínez-Moreno et al.



143 **Figure 1.** Snapshot of surface kinetic energy (\overline{KE}), surface eddy kinetic energy (\overline{EKE}),
 144 surface coherent eddy kinetic energy (\overline{CEKE}), and surface non-coherent eddy kinetic energy
 145 (\overline{nCEKE}) for the 1st of January 2017.

138 (2019). A global snapshot of each component of kinetic energy decomposition is shown
 139 in Figure 1, where the KE and EKE are comprised of rings and filaments. As expected,
 140 the decomposition of EKE into CEKE and nCEKE components exhibit only ring-like
 141 signatures expected of coherent eddies, while the non-coherent component shows filaments
 142 and some miss-identified coherent eddies.

146 2.2 Eddy statistics

147 The eddy statistics used in this study include (i) the eddy count ($cEddy_n$) defined
 148 as the number of eddies per grid cell, (ii) the eddy diameter defined as the diameter of

a circle with equal area as the closed contour of each identified eddy, and (iii) the mean eddy amplitude defined as the mean amplitude of the coherent eddies within the cell ($cEddy_{amp}$). The latter metric can be separated into positive ($cEddy_{amp}^+$) and negative ($cEddy_{amp}^-$) coherent eddy amplitudes, defined as the mean amplitude of warm core and cold core coherent eddies, respectively, within the cell. The absolute eddy amplitude ($|cEddy_{amp}|$) is then defined as:

$$|cEddy_{amp}| = \frac{1}{2} (cEddy_{amp}^+ - cEddy_{amp}^-) \quad (2)$$

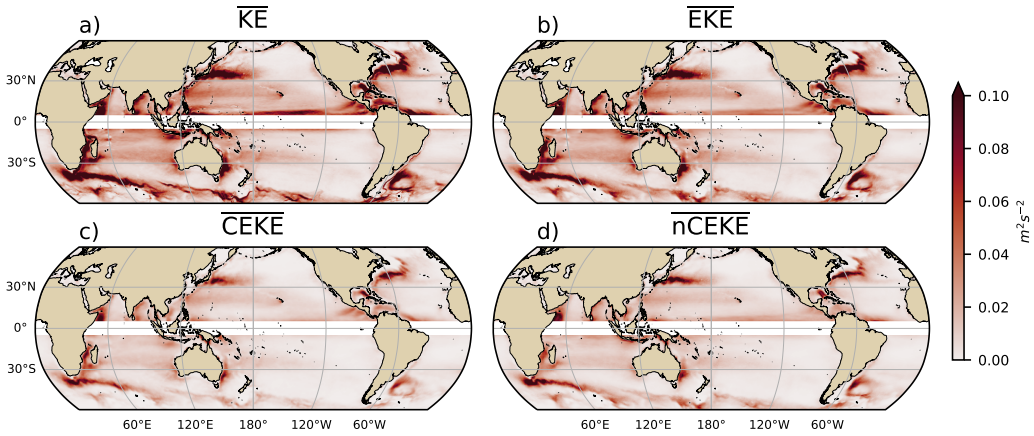
Note that the $cEddy_{amp}^+$ and $cEddy_{amp}^-$ are sign definite, thus the difference will always be positive, mean $cEddy_{amp}$ can be negative or positive noting the dominant polarity of coherent eddies in the region. We analyze the climatology, seasonal cycles and trends of the eddy statistics between 1993 and 2019. We exclude the equatorial region (10°S - 10°N) and poleward of 60° . Note that the climatology of $cEddy_n$ is computed by adding all the identified eddies over the record, while all other climatological statistics are computed as the time-average over the record. Seasonal climatologies are calculated for the monthly average of each coherent eddy statistic, while hemispherical time-series are filtered with a running average of 90 days. Trends of $cEddy_n$ and $|cEddy_{amp}|$ are calculated by coarsening the dataset to a 5° grid, and then linear trends are computed for each grid point, the statistical significance is assessed by a modified Mann-Kendall test (Yue & Wang, 2004).

Time averages are denoted by $\overline{}$, while area-weighted averages are denoted using $\langle \rangle$, the area weighted of function f is:

$$\langle f \rangle = \frac{\int f dx dy}{\int dx dy} \quad (3)$$

3 Global Coherent Eddy Energetics

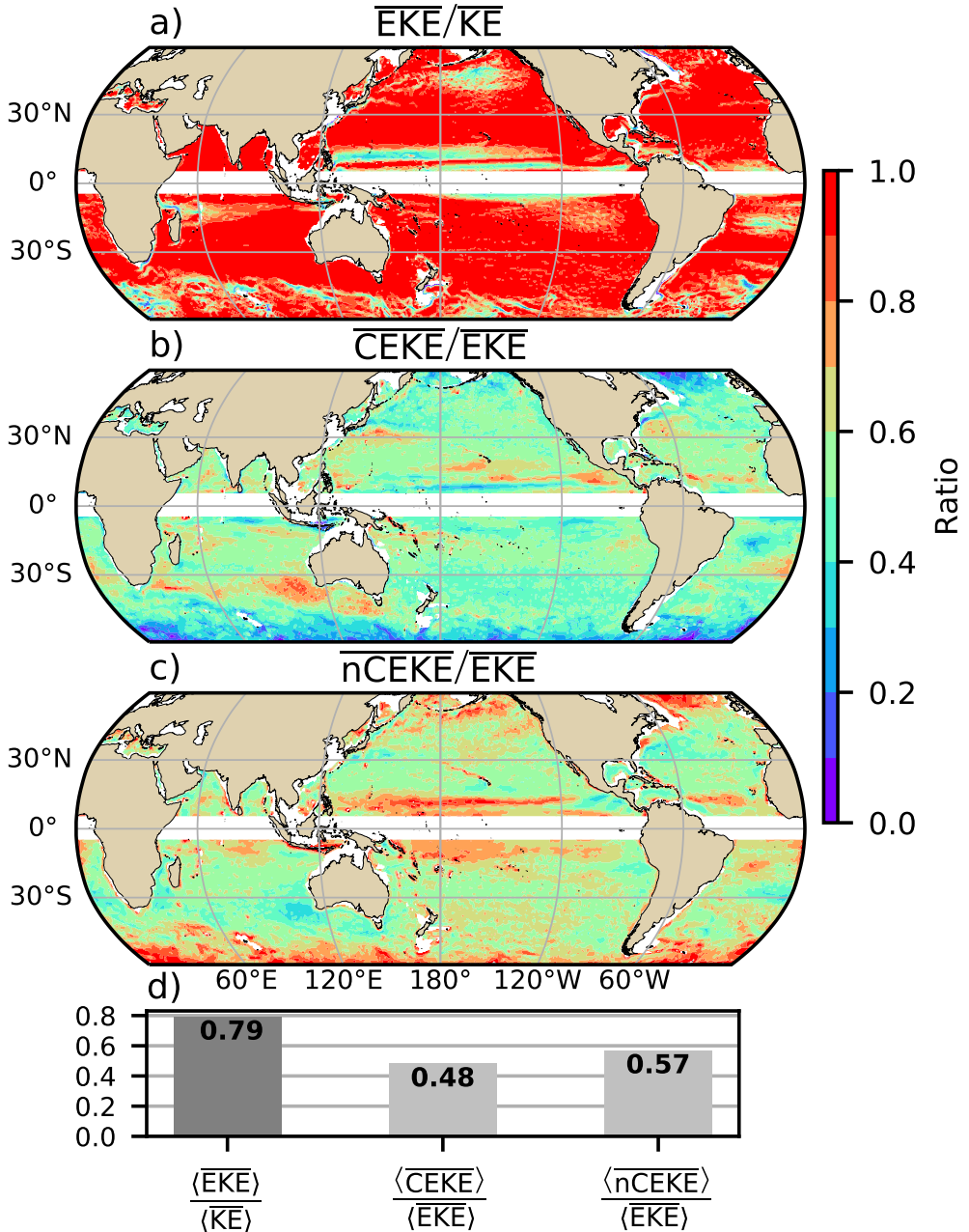
The kinetic energy decomposition estimated from sea surface height measured by satellite altimeters is shown in Figure 2. These maps show that many regions of the global ocean are highly energetic in mean KE (\overline{KE}), mean EKE (\overline{EKE}), mean coherent eddy kinetic energy (\overline{CEKE}) and mean non-coherent eddy kinetic energy (\overline{nCEKE}). The spatial pattern highlights well known regions of the ocean where mesoscale processes are abundant, such as the western boundary extensions and the Antarctic Circumpolar Current. Remarkably, the spatial distribution of the energy contained by the reconstructed mesoscale coherent eddies and non-coherent components are similar (Figures 2c,d). However, there



182 **Figure 2.** Mean surface kinetic energy (\overline{KE}), surface eddy kinetic energy (\overline{EKE}), surface
183 coherent eddy kinetic energy (\overline{CEKE}), and surface non-coherent eddy kinetic energy (\overline{nCEKE})
184 between 1993-2018.

178 are some regions where coherent eddies dominate over non-coherent, and vice-versa. Over-
179 all, this decomposition suggest that boundary current extensions and other energetic re-
180 gions, in particular, eddy-rich regions in the ocean contain both coherent and non-coherent
181 components of the kinetic energy.

194 Eddy kinetic energy is known to be more than an order of magnitude greater than
195 MKE (Gill et al., 1974); this result is clearly shown in Figure 3a, where \overline{EKE} is respon-
196 sible for almost all the \overline{KE} across the ocean, except for regions with persistent currents
197 over time. Such regions are located in the mean boundary extension locations, the equa-
198 torial Pacific currents and regions in the Antarctic Circumpolar Current, where the \overline{EKE}
199 explains around 40% of the \overline{KE} . In a previous study, Chelton et al. (2011) estimated that
200 the EKE within coherent eddies with lifetimes greater than 4 weeks contain between 40
201 to 60 percent of the \overline{EKE} . Our method to reconstruct the coherent eddy signature (Fig-
202 ure 3b) further corroborates that the coherent component (\overline{CEKE}) has $\sim 48\%$ of the \overline{KE}
203 (Figure 3d). Furthermore, global area averages of the ratios show \overline{EKE} explains $\sim 78\%$
204 of the ocean \overline{KE} field, while non coherent eddy features contain $\sim 57\%$ percent of the \overline{EKE} .
205 Note the globally averaged coherent and non coherent components do not add to 100%
206 as the cross terms (\mathcal{O}_c^2) are non-zero, due to coherent eddy reconstruction errors. The
207 spatial pattern reveals a dominance of the \overline{CEKE} equatorward from the boundary ex-
208 tensions and areas with large coherent eddy contributions of around 80% of the region's



185 **Figure 3.** Ratios of the kinetic energy components. a) Map of the proportion of mean eddy
 186 kinetic energy (\overline{EKE}) versus mean kinetic energy (\overline{KE}); b) Map of the percentage of mean co-
 187 herent eddy kinetic energy (\overline{CEKE}) versus mean eddy kinetic energy (\overline{EKE}); c) Map of the
 188 percentage of mean non-coherent eddy kinetic energy (\overline{nCEKE}) versus mean eddy kinetic energy
 189 (\overline{EKE}); d) Global time and area averaged (represented by $\langle \rangle$) percentage of mean eddy kinetic
 190 energy ($\langle \overline{EKE} \rangle$) versus the global mean kinetic energy ($\langle \overline{KE} \rangle$), area averaged percentage of mean
 191 coherent eddy kinetic energy ($\langle \overline{CEKE} \rangle$) and mean non-coherent eddy kinetic energy ($\langle \overline{nCEKE} \rangle$)
 192 versus global mean eddy kinetic energy ($\langle \overline{EKE} \rangle$). Regions where the depth of the ocean is shall-
 193 lower than 1000m are removed from the ratio estimation.

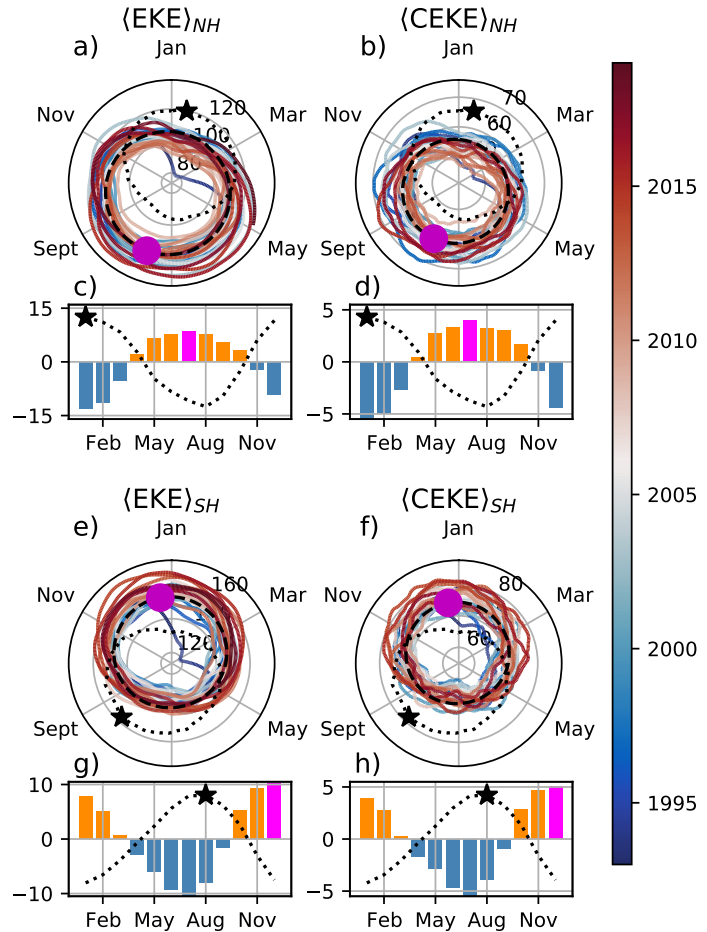
209 eddy kinetic energy can be found south of Australia, the Tehuantepec Gulf, and the trop-
 210 ical Atlantic. An evident signal is an reduction of the energy contained by coherent ed-
 211 dies at high latitudes and an increase in the energy explained by non-coherent eddies;
 212 this signal could be a consequence of the incapability of the 0.25° satellite resolution (\sim
 213 13 km at 60°) to resolve coherent eddies with scales smaller than ~ 10 km (first baro-
 214 clinic Rossby radius at 60° ; Chelton et al. 1998).

215 Figure 4 shows the seasonal cycle of the area weighted EKE and CEKE for the North-
 216 ern Hemisphere ($\langle \text{EKE} \rangle_{NH}$ and $\langle \text{CEKE} \rangle_{NH}$; 10°N - 60°N) and Southern Hemisphere
 217 ($\langle \text{EKE} \rangle_{SH}$ and $\langle \text{CEKE} \rangle_{SH}$; 60°S - 10°S). In both hemispheres, the EKE and CEKE peak
 218 during summer. In the Northern Hemisphere, the largest EKE and CEKE occurs in July,
 219 ~ 6 months after the maximum winds in January (purple bar and back star in Figure 4c
 220 and d). Meanwhile, the Southern Ocean EKE and CEKE seasonal maxima arises dur-
 221 ing December, ~ 4 months after the maximum winds in August (purple bar and back star
 222 in Figure 4g, and h). This lag between winds and the eddy and coherent eddy energy
 223 components is further discussed in section 4.

224 The cyclic plots in Figure 4 show the temporal evolution of EKE and CEKE. Note
 225 that high frequency variability can be observed in the CEKE field with temporal scales
 226 of a few months, this could be attributed local dynamics averaged over the hemisphere,
 227 as well as errors within the coherent eddy reconstruction. Additionally, concentric changes
 228 in the cyclic plots highlight long-term changes over the record. For example, the North-
 229 ern Hemisphere winters in early years of the record (blue) had a more energetic coher-
 230 ent eddy field, which has transitioned to weaker coherent energy contents since 2010 (red),
 231 in other words, the intensity of the CEKE field has decreased. A larger long-term change
 232 can be observed in the Southern Hemisphere, where concentric growth over time in EKE
 233 and CEKE support the previously observed strengthening of the eddy field in the South-
 234 ern Ocean (Hogg et al., 2015; Martínez-Moreno et al., 2019; Martínez-Moreno et al., 2021).

244 4 Global Coherent Eddy Statistics

245 Coherent eddy kinetic energy allows us to quantify and study the energy of the eddy
 246 field, but the coherent eddy properties computed by automated coherent eddy identi-
 247 fication algorithms allow us investigate in more detail the contribution and temporal changes
 248 of their abundance (the number of eddies) and their intensity (both their amplitude and

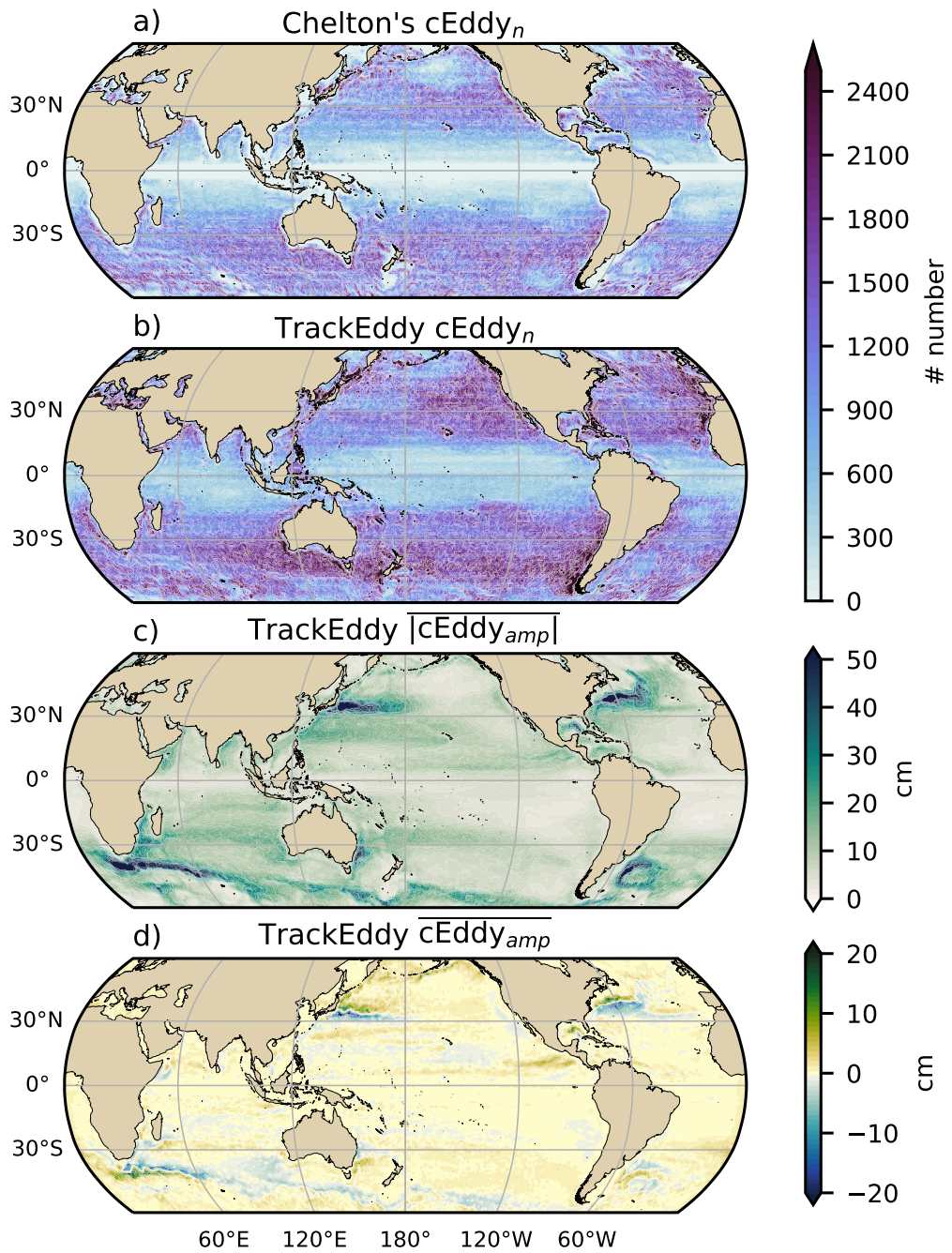


235 **Figure 4.** Seasonality of the area weighted eddy kinetic energy ($\langle EKE \rangle$), coherent eddy ki-
 236 netic energy ($\langle CEKE \rangle$). Panels a and b show the time-series of the Northern Hemisphere, while
 237 panels e and f correspond to the Southern Hemisphere. Panels c and d show the seasonal cycle of
 238 the $\langle EKE \rangle_{NH}$ and $\langle CEKE \rangle_{NH}$ in the Northern Hemisphere, and panels g and h show the South-
 239 ern Hemisphere ($\langle EKE \rangle_{SH}$ and $\langle CEKE \rangle_{SH}$). Dashed lines correspond to the seasonal cycle of the
 240 fields and dotted lines show the seasonal cycle of the wind magnitude smoothed over 120 days
 241 (moving average). The black and magenta markers (circle and bar) show the maximum of the
 242 seasonal cycle for the kinetic energy components and the wind magnitude, respectively. In cyclic
 243 plots, line colors shows the year.

diameter). Figure 5 shows gridded climatologies of the number of eddies and the eddy amplitude. We contrast our M-M eddy count with Chelton et al. (2007) (Figure 5a-b). Although the number of the identified eddies is larger in M-M, possibly due to the lifespan filter implemented by Chelton, both datasets reveal consistent spatial patterns. For example, both datasets show high abundance of eddies in the East North Pacific, East North Atlantic, as well as the East South Pacific, East South Atlantic and East Indian Ocean, and small number counts of eddies in the tropics and in high latitudes ($\sim 60^\circ$). An interesting pattern also emerges in both eddy count datasets, where small scale structures with larger eddy counts are favored across the ocean. In addition, to preferential coherent eddy paths observable in boundary extensions and regions in the Southern Ocean. These clusters and paths of coherent eddies could be associated with topographic features, however they remain a puzzling consistency between the eddy count pattern using these two eddy identification methods.

Regions with large counts of eddies have in general small absolute amplitudes (Figure 5 c), ocean gyre interiors follow with a larger absolute amplitude and finally regions such as the boundary extensions and Antarctic Circumpolar Current have the largest coherent eddy absolute amplitudes as shown by Chelton et al. (2011). Eddy amplitude highlights regions dominated by a given coherent eddy polarity, for example, boundary extensions have a preferred sign (Figure 5 d); positive amplitude polewards of the boundary extension mean location, and negative amplitude equatorwards. This sign preference is consistent with the preferential way coherent eddies are shed from boundary extensions; warm core eddies (positive) polewards of the boundary current extension, and equatorward for cold core eddies (negative) (Kang & Curchitser, 2013; Chelton et al., 2011, 2007). These global statistics reveal the absolute coherent eddy amplitude is a proxy of the CEKE with similar spatial patterns (Figure 2 & Figure 5 c) and showcases that regions where $\overline{\text{CEKE}}$ has a large proportion of $\overline{\text{EKE}}$ (Figure 3), the absolute coherent eddy amplitude is also large.

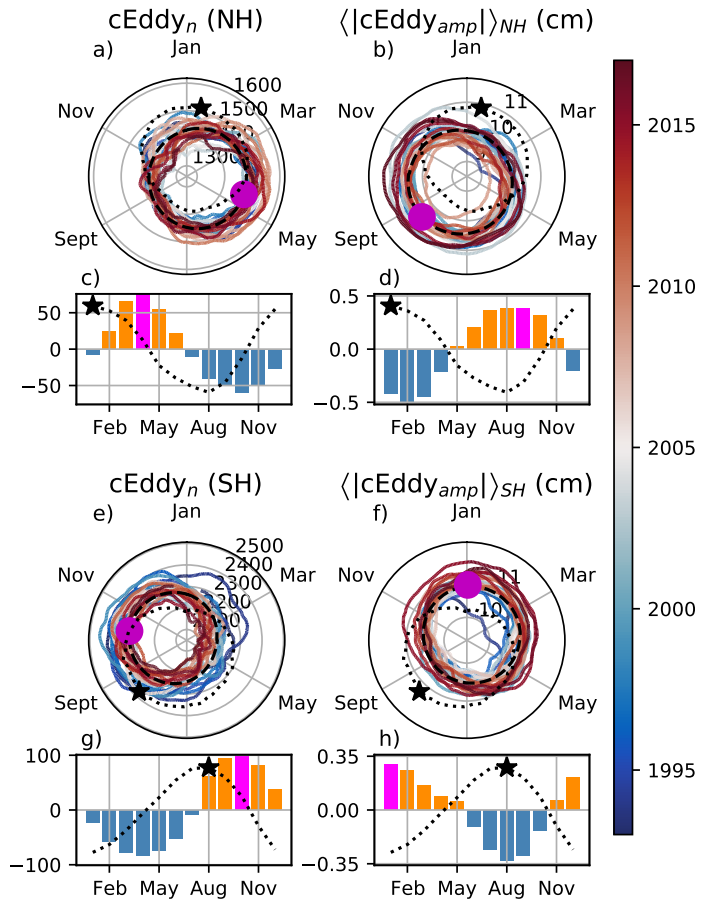
To further understand the seasonal cycle of CEKE, we compute the climatology of coherent eddy properties in each hemisphere (Figure 6). The seasonality of the number of eddies in the Northern Hemisphere peaks on April (Figure 6 a, c), while the Southern Hemisphere maximum number of eddies occurs during October (Figure 6 e, g). Meanwhile, the seasonality of the absolute eddy amplitude peaks in August and January for the Northern and Southern Hemispheres respectively (Figure 6 b, d, f, and h). As ex-



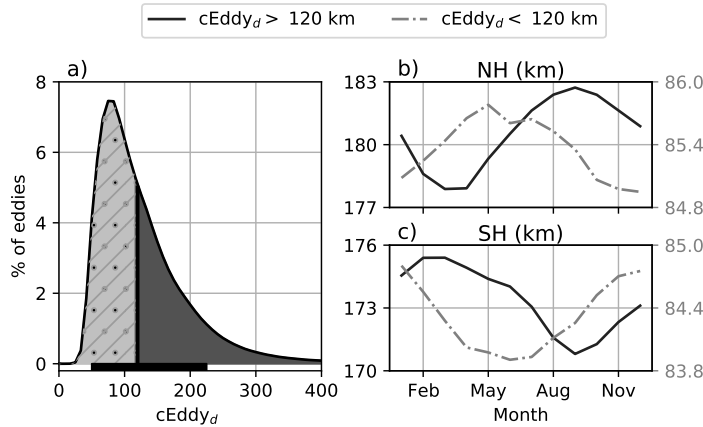
262 **Figure 5. Check** $|cEddy_{amp}|$ Averaged coherent eddy statistics. a) Climatology of the
 263 number of coherent eddies ($cEddy_n$) identified by Chelton et al. (2007); b) Climatology of the number
 264 of coherent eddies ($cEddy_n$) identified by Martínez-Moreno et al. (2019); c) Climatology of the
 265 mean absolute coherent eddy amplitude ($cEddy_{amp}$). d) Climatology of the mean coherent eddy
 266 amplitude ($cEddy_{amp}$).

287 pected, the seasonality of the absolute eddy amplitude, or intensity of the coherent ed-
288 dies, is consistent with the seasonal cycle of CEKE. Furthermore, a distinct lag of ~ 3
289 months is observed between the winds and eddy count, while the eddy amplitude max-
290 imum occurs ~ 6 months after the seasonal maxima in winds. We observe the eddy num-
291 ber increases earlier in the year and through eddy-eddy interactions (merging of coher-
292 ent eddies) the amplitude of the coherent eddy increases ~ 3 months after. This seasonal
293 lag and summer maxima is consistent with Figure 5, furthermore, previous studies sug-
294 gest that a time-lag of the inverse cascade (Sasaki et al., 2014; Qiu et al., 2014) is respon-
295 sible of the EKE seasonal cycle, where winter has the highest energy at the smallest scales
296 (non-resolvable with satellite observations), spring and autumn have the highest and low-
297 est energy in scales of 50-100 km, and summertime has the highest energy at the largest
298 scales (> 100 km; Uchida et al. 2017). Thus, the maximum of EKE, CEKE, and $\langle |cEddy_{amp}| \rangle$
299 located during summertime suggest that the seasonality of eddies and coherent eddies
300 could be dominated by scales larger than 100 km. This result can be further explored
301 by looking at the seasonal evolution of the eddy diameter. Note that 90% of identified
302 coherent eddies have diameters between 50 to 220 km (Figure 7 a). We divided eddies
303 into large-scale coherent eddies (diameter > 120 km) and small-scale coherent eddies (di-
304 ameter < 120 km; Figure 7a). In the Northern Hemisphere, small eddies have a seasonal
305 peak in diameter during May, while large eddies have the greatest diameter in Septem-
306 ber (Figure 7 b). Meanwhile, in the Southern Hemisphere, the small-scale coherent ed-
307 dies have the maximum diameter in December, while large-scale coherent eddies peak
308 in February (Figure 7 c). This result suggests that wind driven baroclinic instabilities
309 generate small coherent eddies early in the season, which then merge and grow to be-
310 come larger in diameter and amplitude, and thus, more energetic. This process is asso-
311 ciated with the inverse energy cascade, and suggest that this mechanism not only drives
312 the EKE seasonality, but also may be responsible of the seasonal cycle of coherent ed-
313 dies.

314 Long-term changes can be observed in Figure 6a,b, e, and f where growing-shrinking
315 concentric circles over time denote an increase-decrease trend of the field. This trend is
316 particularly evident in the Southern Hemisphere, where the number of eddies has decreased,
317 the eddy amplitude has increased. This result is consistent with the observed trends in
318 EKE and mesoscale EKE in the Southern Ocean (Hogg et al., 2015; Martínez-Moreno
319 et al., 2019).



320 **Figure 6.** Check $\langle |c\text{Eddy}_{amp}| \rangle$ Hemispherical seasonality of the coherent eddy statistics;
 321 a,e) seasonal cycle of the number of coherent eddies ($c\text{Eddy}_n$); b,f) seasonal cycle of the area
 322 weighted coherent eddy amplitude ($\langle |c\text{Eddy}_{amp}| \rangle$); c,g) seasonal cycle of the warm core coherent
 323 eddies amplitude (positive $c\text{Eddy}_{amp}$); d,h) seasonal cycle of the cold core coherent eddies ampli-
 324 tude (negative $c\text{Eddy}_{amp}$). Panels a,b and c show the Northern Hemisphere seasonal cycle, while
 325 panels d,e, and f correspond to the Southern Hemisphere. Dashed lines correspond to the sea-
 326 sonal cycle of the fields and dotted lines show the seasonal cycle of the wind magnitude smoothed
 327 over 120 days (moving average). The green and magenta stars show the maximum of the seasonal
 328 cycle for each field and the wind magnitude, respectively. The line colors show the year.



329 **Figure 7.** Distribution of the identified eddy diameter ($cEddy_d$; km) and hemispherical
 330 seasonality of the coherent eddy diameter. a) Distribution in percentage of identified eddy am-
 331 plitude, solid bar below distribution represents 90% of the identified eddies. Seasonal cycle of
 332 the eddy diameter for the b) Northern Hemisphere and c) Southern Hemisphere. Dark solid line
 333 and area corresponds to coherent eddies with diameters larger than 120 km, while light gray
 334 dash-dotted line and area shows coherent eddies with diameters smaller than 120 km.

335 The coherent eddy amplitude from positive coherent eddies and negative coherent
 336 eddies show similar seasonal cycles to the absolute eddy amplitude. The Northern Hemis-
 337 phere decrease in absolute eddy amplitude is driven by a decrease of the amplitude of
 338 negative coherent eddies in the Northern Hemisphere. Meanwhile in the Southern Ocean,
 339 the increase in absolute eddy amplitude is corroborated by an strengthening of both co-
 340 herent eddy polarities since the early 90s.

341 5 Trends

342 The results presented in Figures 4 and 6 suggest a long-term readjustment of the
 343 coherent eddy field. The long-term trends of the number of coherent eddies, absolute co-
 344 herent eddy amplitude, and coherent eddy amplitude polarities are explored in Figure
 345 8. Chelton's and M-M datasets show consistent spatial patterns in the trends and sig-
 346 nificance of the number of coherent eddies and the absolute coherent eddy amplitude.
 347 Several regions in the ocean, such as the Southern Ocean, North Atlantic and North Pa-
 348 cific, show a decrease in the number of eddies. Those same regions also have a clear in-
 349 crease in the absolute coherent eddy amplitude. These trends are similar to those ob-

350 served in mesoscale eddy kinetic energy (Martínez-Moreno et al., 2021) and provide ad-
351 dditional evidence of a readjustment of the mesoscale eddy field over the last 3 decades.

352 *@Matt: What do you think? Is it important to highlight the trends we observe are
353 different to sea level rise? Or is the next paragraph irrelevant?*

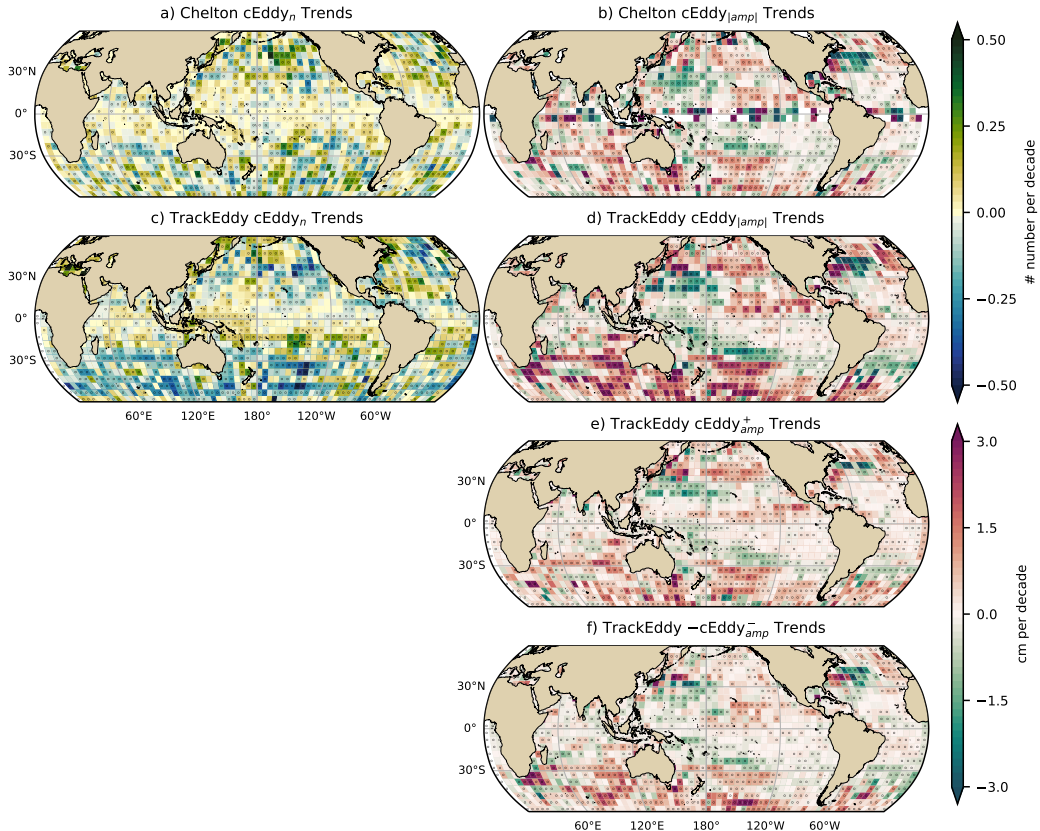
354 The observed trends of $|cEddy_{amp}|$ in several oceanic regions have the same scale
355 as sea level rise ($\sim 3\text{cm}$ per decade) by analyzing the positive and negative coherent eddy
356 amplitude we can discard the observed trends correspond to an increase in sea level. In
357 fact, each coherent eddy polarity has intensified in the Southern Ocean and North East
358 Pacific and Atlantic. In other words, the absolute amplitude of each polarity has increased
359 over time, thus this strengthening is an intrinsic response of the coherent eddy field. Note
360 that the negative coherent eddy amplitude dominates the global $|cEddy_{amp}|$ trends (Figure
361 8e, f). However, different trend pattern can be observed in both positive and neg-
362 ative coherent eddy amplitudes in the north Atlantic and north Pacific, where the neg-
363 ative coherent eddy amplitude in the Western Boundary Currents appears to decrease.

371 6 Regional Climatology

372 For regions with relatively large proportions of CEKE located at boundary exten-
373 sions and eastern currents, we investigate the seasonal and long-term variability of the
374 coherent eddy properties.

375 The most energetic western boundary extensions include; the Gulf Stream, the Kuroshio
376 Current, and the Agulhas Current (Figures 9, 10, and 11). Coherent eddy generation in
377 boundary extensions occurs through baroclinic and barotropic instabilities of the mean
378 current, thus all these regions share similar generation dynamics. In all these regions with-
379 out exception; (i) CEKE contains up to 80% of the EKE in regions equatorwards from
380 the mean western boundary extension location, (ii) the number of eddies is consistently
381 minimal numbers of eddies over the mean western boundary extension location, and (iii)
382 the absolute eddy amplitude is larger polewards of the mean western boundary exten-
383 sion location.

384 In the Gulf Stream, the energy ratio between CEKE and EKE is $\sim 56\%$ (Figure 9).
385 The highest energy content occurs in regions with numerous eddies, and collocated with
386 regions where the largest $|cEddy_{amp}|$ gradients occurs. The time series of $cEddy_n$ and
387 $|cEddy_{amp}|$ are anti-correlated (-0.52), and they display inter-annual and seasonal vari-



364 **Figure 8. Should we use $\langle \text{cEddy}_{amp} \rangle$? or only change to $\text{cEddy}_{|amp|}$?** Trends of co-
 365 herent eddy statistics. a) and b) Trends of the number of identified coherent eddies from satellite
 366 observations identified using TrackEddy, and those reported in Chelton's dataset. c) and d)
 367 Trends of the mean absolute value of identified coherent eddies amplitude from satellite obser-
 368 vations identified using TrackEddy, and those reported in Chelton's dataset. e) and f) Trends
 369 of eddy amplitude polarity using TrackEddy. Gray stippling shows regions that are statistically
 370 significant above the 95% confidence level. **Change $\text{cEddy}_{|amp|}$ to $|\text{cEddy}_{amp}|$**

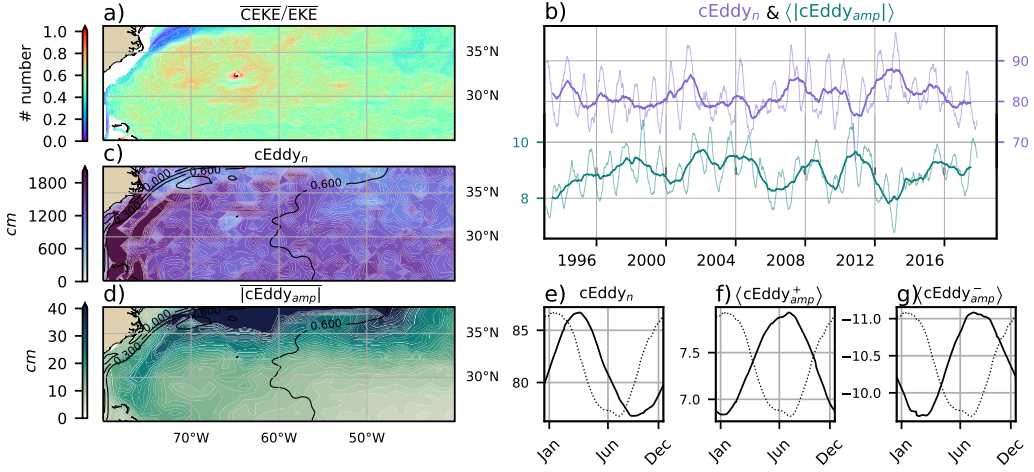


Figure 9. Climatology of the eddy field and coherent eddy field at the Gulf Stream. a) Ratio of mean coherent eddy kinetic energy ($\overline{\text{CEKE}}$) versus mean eddy kinetic energy ($\overline{\text{EKE}}$); b) Thick lines show the running average over 2 years and thin lines show the running average over 90 days of the coherent eddy number sum and the average absolute coherent eddy amplitude; c) Map of the number of eddies; d) Map of the average absolute coherent eddy amplitude; e) Seasonal cycle of the number of eddies f) Seasonal cycle of the positive coherent eddy amplitude. g) Seasonal cycle of the negative coherent eddy amplitude. Contours in maps correspond to mean sea surface height (m).

ability. Although Chaudhuri et al. (2009) observed a positive phase of North Atlantic Oscillation (NAO) exhibit higher EKE, due to an increase in baroclinic instabilities, thus suggesting more coherent eddies, we do not find a correlation between the $c\text{Eddy}_n$ or the $|c\text{Eddy}_{amp}|$ in the Gulf Stream and the NAO index. Similar to the signal observed in the hemispherical analysis, the eddy count seasonal cycle follows the wind maximum after ~ 3 months, while the amplitude of the coherent eddies lags by ~ 6 months.

The variability of the $c\text{Eddy}_n$ and $|c\text{Eddy}_{amp}|$ in the Kuroshio Current are weakly anti-correlated (-0.41; Figure 10). However, on average 56% of the energy in the region corresponds to CEKE. As observed in the Gulf Stream, there is an important seasonal cycle in the boundary extensions, where the eddy count seasonal cycle occurs on March after ~ 3 months of the wind maximum (January). Meanwhile, the amplitude of the coherent eddies lags by ~ 6 months (June) after the maximum wind.

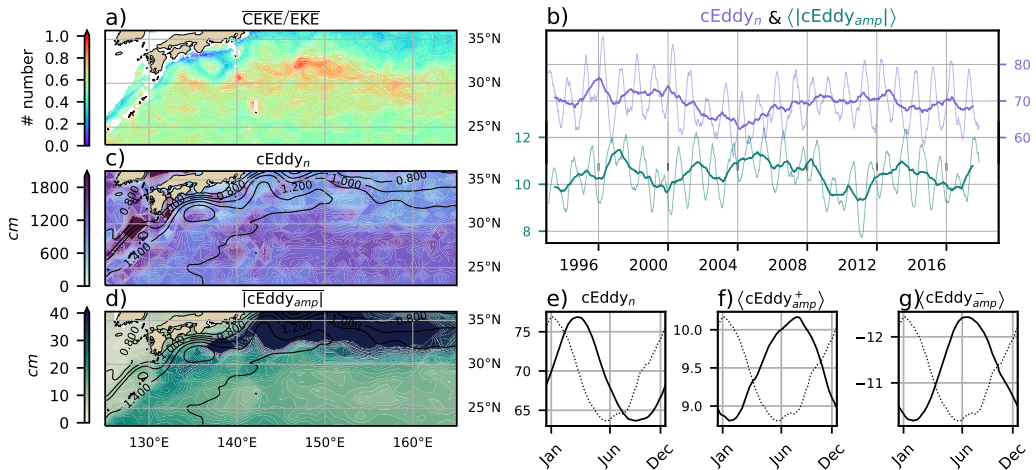


Figure 10. Climatology of the eddy field and coherent eddy field at the Kuroshio extension.
 a) Ratio of mean coherent eddy kinetic energy ($\overline{\text{CEKE}}$) versus mean eddy kinetic energy ($\overline{\text{EKE}}$);
 b) Time-series of the coherent eddy number and the average absolute coherent eddy amplitude;
 c) Map of the number of eddies; d) Map of the average absolute coherent eddy amplitude; Seasonal cycle of the e) number of eddies, f) positive coherent eddy amplitude, and g) negative coherent eddy amplitude. Different lines represent the same as in Figure 9.

In the Southern Hemisphere, the strongest boundary current, the Agulhas Current shows similar behavior to its counterparts in the Northern Hemisphere (Figure 11). On average, coherent eddies in the Agulhas current contain $\sim 56\%$ of the energy, meanwhile the cEddy_n seasonal peak occurs in August, while the $|\text{cEddy}_{amp}|$ occurs in January–February. The seasonal lag between the winds, eddy count, and eddy amplitude in each of the western boundary current extensions is interpreted as being analogous to the explanation observed in Figure 6 of the lagged response of coherent eddy properties due to eddy-eddy interactions, consistent with the inverse cascade of energy.

Coherent eddies dominate the EKE field in other regions such as the Leeuwin Current (Figure 12), where the 65% of the energy is contained by coherent eddies. Although the Leeuwin region is not characterized by having a large EKE, however, a considerable abundance of eddies and large eddy amplitudes are observable in the region. The series reveal a significant increase in the $|\text{cEddy}_{amp}|$, while the cEddy_n has decreased over the last 3 decades (). The seasonal cycle shows that the cEddy_n peak occurs on August, 3

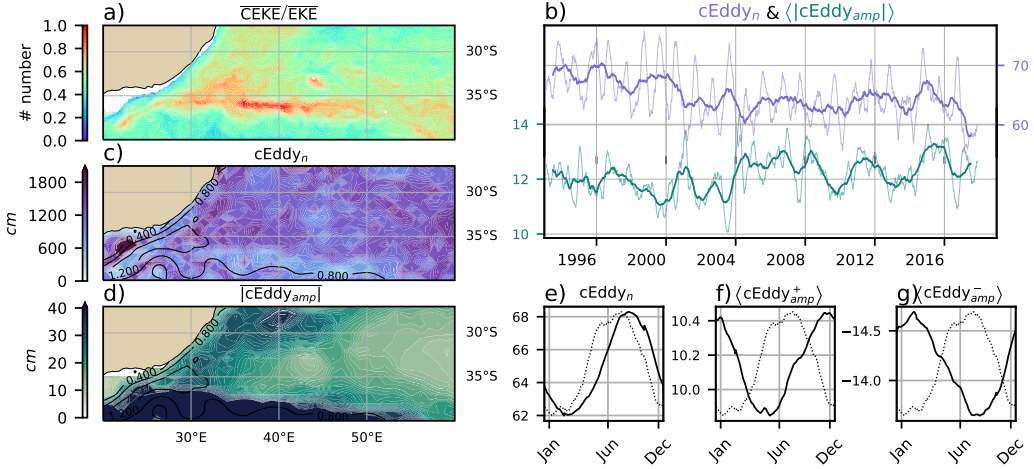
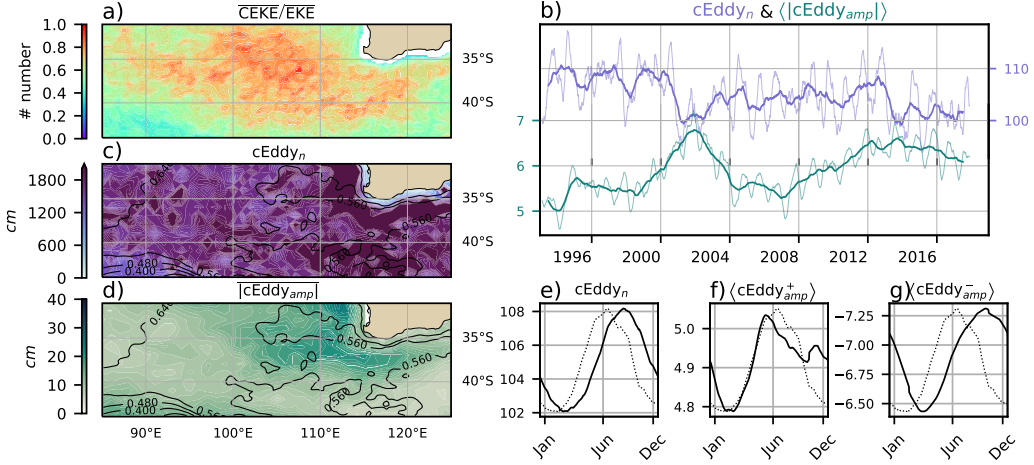


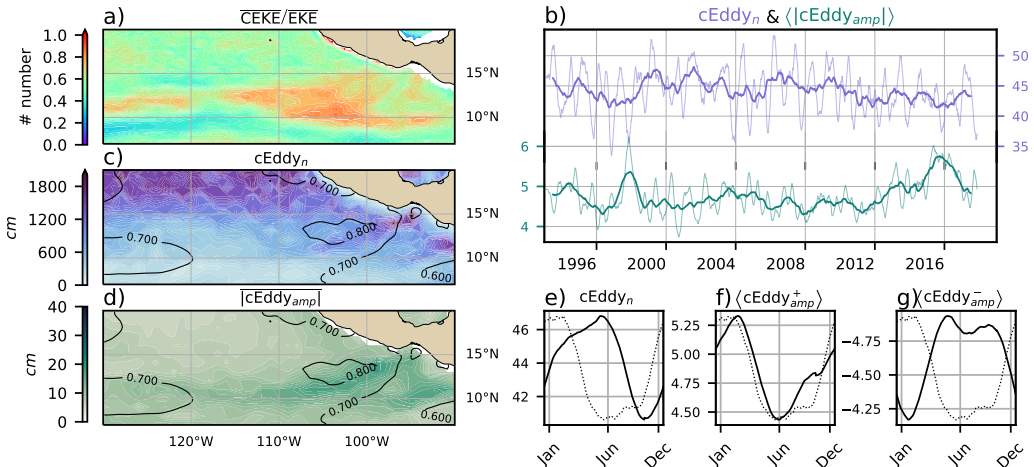
Figure 11. Climatology of the eddy field and coherent eddy field at the Agulhas Current. a) Ratio of mean coherent eddy kinetic energy ($\overline{\text{CEKE}}$) versus mean eddy kinetic energy ($\overline{\text{EKE}}$); b) Time-series of the coherent eddy number and the average absolute coherent eddy amplitude; c) Map of the number of eddies; d) Map of the average absolute coherent eddy amplitude; Seasonal cycle of the e) number of eddies, f) positive coherent eddy amplitude, and g) negative coherent eddy amplitude. Different lines represent the same as in Figure 9.

months after the maximum winds (June). Meanwhile, the cEddy_{amp}^+ responds in synchrony to winds, and the cEddy_{amp}^- is in phase with the seasonal cycle of the cEddy_n .

Another region with important contributions of the coherent eddy field is the East Tropical Pacific (Tehuantepec region; Figure 13), where coherent eddies contain $\sim 58\%$ of the energy. In fact, coherent eddy generation in this region is modulated by winds and coastally trapped waves which produce a strong horizontal and vertical shear (baroclinic and barotropic instabilities; Zamudio et al., 2006). Furthermore, the equatorial generated waves propagating along the coast have an important interannual variability observable in the $|\text{cEddy}_{amp}|$ time-series, where El Niño events are notable during 1997 and 2015 (Figure 13b). The seasonal cycle of cEddy_n , cEddy_{amp}^+ , and cEddy_{amp}^- support the idea of a coherent eddies responding to two different coherent eddy generation mechanisms; the number of eddies seasonal cycle lags for by ~ 3 months from the winds, while the cEddy_{amp}^+ is on phase with the winds and the maximum of trapped waves (winter; Zamudio et al., 2006), and the cEddy_{amp}^- could be a consequence of eddy-eddy interactions.



436 **Figure 12.** Climatology of the eddy field and coherent eddy field at the Leeuwin Current. a)
437 Ratio of mean coherent eddy kinetic energy (\overline{CEKE}) versus mean eddy kinetic energy (\overline{EKE}); b)
438 Time-series of the coherent eddy number and the average absolute coherent eddy amplitude; c)
439 Map of the number of eddies; d) Map of the average absolute coherent eddy amplitude; Seasonal
440 cycle of the e) number of eddies, f) positive coherent eddy amplitude, and g) negative coherent
441 eddy amplitude. Different lines represent the same as in Figure 9.



455 **Figure 13.** Climatology of the eddy field and coherent eddy field at the East Tropical Pacific.
456 a) Ratio of mean coherent eddy kinetic energy (\overline{CEKE}) versus mean eddy kinetic energy (\overline{EKE});
457 b) Time-series of the coherent eddy number and the average absolute coherent eddy amplitude;
458 c) Map of the number of eddies; d) Map of the average absolute coherent eddy amplitude; Sea-
459 sonal cycle of the e) number of eddies, f) positive coherent eddy amplitude, and g) negative
460 coherent eddy amplitude. Different lines represent the same as in Figure 9.

461 **7 Discussion and Conclusions**

462 We investigated the contribution of coherent eddies in the kinetic energy field us-
 463 ing satellite observations. We corroborate that around half of the EKE is explained by
 464 coherent eddies. This half is concentrated in eddy-rich regions where an intensification
 465 of the eddy field has been observed (Martínez-Moreno et al., 2021). The energy contained
 466 by eddies is larger than the previous estimate of 40% by Chelton et al. (2011). Although
 467 there are difference in the identification criteria of both eddy identification methods, the
 468 main cause of the difference is believed to be the lifespan and amplitude filters. These
 469 filters are widely used to track individual eddies on space and time, however, interactions
 470 between eddies in energetic regions my obscure the abundance and influence of short-
 471 lived coherent eddies. Filters are not used in this study, and indeed a lack of filters could
 472 facilitates an under or over-estimation of the the energy contained by coherent eddies,
 473 when miss-identifying or miss-fitting a coherent eddy. Thus, the presented estimate rep-
 474 resents an upper limit of the energy contained by coherent eddies.

475 In addition, it should be noted that regions with first baroclinic Rossby radius of
 476 deformation smaller than 10km cannot be resolved by satellite observations. Thus, the
 477 energy contained by coherent eddies around latitudes of 60° and those near the shore
 478 are missed from this estimate, and remains unknown their role in the seasonal cycle and
 479 local dynamics. New satellite altimeter missions (SWOT) may allow to estimate energy
 480 contained by mesoscale coherent eddies outside the tropical region and the continental
 481 slope.

482 Hemispherical variability indicates a strong seasonal cycle of the EKE, CEKE, and
 483 eddy properties. The seasonal cycle of the CEKE in each hemisphere occurs as a con-
 484 sequence of numerous small coherent eddies interacting with each other (eddy-eddy in-
 485 teractions) and resulting in stronger, larger and more energetic coherent eddies during
 486 summer after a few months of the yearly coherent eddy number maxima. This results
 487 reveals eddy-eddy interactions and thus the transfer of energy from smaller coherent ed-
 488 dries to larger coherent eddies could explain the observed seasonal cycle of CEKE and
 489 coherent eddies properties.

490 Coherent eddy properties showcase a non-uniform long-term readjustment of the
 491 mesoscale eddy field. Overall, the eddy number has decreased globally at a significant
 492 rate of ~ 35 eddies per decade from ~ 4000 eddies identified globally on average each day.

493 However, large proportions of the ocean show an strengthening of the mesoscale coher-
494 ent eddy field at a rate greater than ~ 1 cm per decade. This strengthening of the co-
495 herent eddy amplitude is attributed to an intensification of each coherent eddy polar-
496 ity, rather than a readjustment of the coherent eddy field to sea level rise. In other words,
497 the coherent eddy amplitude intensification is occurring in both coherent eddy polar-
498 ities and explain a proportion of the previously observed readjustments in the eddy field
499 to long-term changes in the ocean forcing (Hu et al., 2020; Wunsch, 2020; Martínez-Moreno
500 et al., 2021). This long-term readjustment showcases an intensification of the coherent
501 eddy field, possibly due to long-term readjustments in the ocean baroclinic and barotropic
502 instabilities, as well as the strength of the winds.

503 The reconstruction of the coherent eddies and their statistics have revealed regions
504 with important coherent eddy contributions and a distinct seasonal evolution of the co-
505 herent eddies. Remarkably, western boundary extensions generate eddies through the
506 instability of the main currents and the seasonal cycle of coherent eddies, CEKE, and
507 thus EKE could be associated with an inverse energy cascade observable through lagged
508 seasonal cycles in the coherent eddy statistics. In addition to this, the amplitude of the
509 seasonal cycle in the boundary extensions is two times larger than any other region, thus
510 the seasonality of the coherent eddies in boundary extensions dominate the hemispher-
511 ical seasonal cycle. Furthermore, the seasonal lag of the inverse energy cascade is cou-
512 pled with the presence of fronts, such is the case of western boundary extensions, and
513 our results are consistent with the notion of baroclinic instability generating eddies and
514 through eddy-eddy interactions an lagged inverse energy cascade.

515 The use of satellite observations in this study limit our ability to quantify the im-
516 portance of the inverse energy cascade seasonality in the control of the coherent eddy
517 seasonal cycle. As mentioned above, there is robust evidence of an increase in eddy-eddy
518 interactions, however we can not discard important contributions from other processes
519 such as the seasonal cycle of forcing and instabilities, which are crucial in the genera-
520 tion of coherent eddies. Although this study can provide a descriptive response of the
521 coherent eddy field, further studies are needed to asses the role of eddy-eddy interactions
522 in our changing climate, ocean dynamics, and biogeochemical process. Furthermore, the
523 SWOT mission could allow to advance our understanding of eddy-eddy interactions and
524 the seasonal cycle of scales smaller than mesoscale, which may provide further evidence
525 of the inverse energy cascade driving the coherent eddy seasonality.

526 **Acknowledgments**

527 Chelton & Schlax (2013) dataset was produced by SSALTO/DUACS and distributed by
 528 AVISO+ (<https://www.aviso.altimetry.fr/>) with support from CNES, developed
 529 and validated in collaboration with E.Mason at IMEDEA. Global coherent eddy recon-
 530 struction, coherent and non-coherent eddy kinetic energy datasets, in addition to grid-
 531 deded coherent eddy tracking datasets are publicly available at (<https://doi.org/10.5281/zenodo.4646429>). All analyses and figures in this manuscript are reproducible via Jupyter
 532 notebooks and instructions can be found in the Github repository `CEKE_climatology`
 533 (https://github.com/josuemtzmo/CEKE_climatology). Trends used the Python Pack-
 534 age `xarrayMannKendall` (<https://doi.org/10.5281/zenodo.4458776>)

536 **References**

- 537 Arbic, B. K., Polzin, K. L., Scott, R. B., Richman, J. G., & Shriver, J. F. (2013).
 538 On Eddy Viscosity, Energy Cascades, and the Horizontal Resolution of Gridded
 539 Satellite Altimeter Products*. *Journal of Physical Oceanography*, 43(2), 283–300.
 540 doi: 10.1175/jpo-d-11-0240.1
- 541 Ashkezari, M. D., Hill, C. N., Follett, C. N., Forget, G., & Follows, M. J. (2016).
 542 Oceanic eddy detection and lifetime forecast using machine learning methods.
 543 *Geophysical Research Letters*, 43(23). doi: 10.1002/2016gl071269
- 544 Beron-Vera, F. J., Wang, Y., Olascoaga, M. J., Goni, G. J., & Haller, G. (2013). Ob-
 545 jective Detection of Oceanic Eddies and the Agulhas Leakage. *Journal of Physical
 546 Oceanography*, 43(7), 1426–1438. doi: 10.1175/JPO-D-12-0171.1
- 547 Bouali, M., Sato, O. T., & Polito, P. S. (2017). Temporal trends in sea surface tem-
 548 perature gradients in the South Atlantic Ocean. *Remote Sensing of Environment*,
 549 194, 100–114. doi: 10.1016/j.rse.2017.03.008
- 550 Callies, J., Flierl, G., Ferrari, R., & Fox-Kemper, B. (2015). The role of mixed-layer
 551 instabilities in submesoscale turbulence. *Journal of Fluid Mechanics*, 788, 5–41.
 552 doi: 10.1017/jfm.2015.700
- 553 Cane, M. A., Clement, A. C., Kaplan, A., Kushnir, Y., Pozdnyakov, D., Seager, R.,
 554 ... Murtugudde, R. (1997). Twentieth-Century Sea Surface Temperature Trends.
 555 *Science*, 275(5302), 957–960. doi: 10.1126/science.275.5302.957
- 556 Chaudhuri, A. H., Gangopadhyay, A., & Bisagni, J. J. (2009). Interannual variabil-
 557 ity of Gulf Stream warm-core rings in response to the North Atlantic Oscillation.

- 558 *Continental Shelf Research*, 29(7), 856–869. doi: 10.1016/j.csr.2009.01.008
- 559 Chelton, D. B., A. d. R., Schlax, M. G., Naggar, K., & Siwetz, N. (1998). Geographical
560 variability of the first baroclinic Rossby radius of deformation. *Journal*
561 of *Physical Oceanography*, 28(3), 433-460. doi: 10.1175/1520-0485(1998)028<433:
562 GVOTFB>2.0.CO;2
- 563 Chelton, D. B., Gaube, P., Schlax, M. G., Early, J. J., & Samelson, R. M. (2011).
564 The influence of nonlinear mesoscale eddies on near-surface oceanic chlorophyll.
565 *Science*, 334(6054), 328-32. doi: 10.1126/science.1208897
- 566 Chelton, D. B., & Schlax, M. G. (2013). *Mesoscale eddies in altimeter observations*
567 of *ssh*.
- 568 Chelton, D. B., Schlax, M. G., Samelson, R. M., & de Szoeke, R. A. (2007). Global
569 observations of large oceanic eddies. *Geophysical Research Letters*, 34(15),
570 L15606. doi: 10.1029/2007GL030812
- 571 CMEMS. (2017). The Ssalto/Duacs altimeter products were produced and dis-
572 tributed by the Copernicus Marine and Environment Monitoring Service. *Aviso*
573 Dataset. Retrieved from <https://www.aviso.altimetry.fr/>
- 574 Cui, W., Wang, W., Zhang, J., & Yang, J. (2020). Identification and census statis-
575 tics of multicore eddies based on sea surface height data in global oceans. *Acta*
576 *Oceanologica Sinica*, 39(1), 41–51. doi: 10.1007/s13131-019-1519-y
- 577 Faghmous, J. H., Frenger, I., Yao, Y., Warmka, R., Lindell, A., & Kumar, V. (2015,
578 6). A daily global mesoscale ocean eddy dataset from satellite altimetry. *Scientific*
579 *Data*, 2, 150028 EP -. doi: 10.1038/sdata.2015.28
- 580 Ferrari, R., & Wunsch, C. (2009). Ocean Circulation Kinetic Energy: Reservoirs,
581 Sources, and Sinks. *Annual Review of Fluid Mechanics*, 41(1), 253–282. doi: 10
582 .1146/annurev.fluid.40.111406.102139
- 583 Frenger, I., Gruber, N., Knutti, R., & Münnich, M. (2013). Imprint of Southern
584 Ocean eddies on winds, clouds and rainfall. *Nature Geoscience*, 6(8), 608 EP -.
585 doi: 10.1038/ngeo1863
- 586 Frenger, I., Münnich, M., Gruber, N., & Knutti, R. (2015). Southern Ocean eddy
587 phenomenology. *Journal of Geophysical Research: Oceans*, 120(11), 7413-7449.
588 doi: 10.1002/2015JC011047
- 589 Fu, L., Chelton, D., Le Traon, P., & Oceanography, M. R. (2010). Eddy dynamics
590 from satellite altimetry. *Oceanography*, 23(4), 14-25. doi: 10.2307/24860859

- 591 Gill, A., Green, J., & Simmons, A. (1974). Energy partition in the large-scale ocean
 592 circulation and the production of mid-ocean eddies. *Deep Sea Res Oceanogr Abstr*,
 593 21(7), 499-528. doi: 10.1016/0011-7471(74)90010-2
- 594 Hogg, A. M., & Blundell, J. R. (2006). Interdecadal variability of the southern
 595 ocean. *Journal of Physical Oceanography*, 36(8), 1626-1645. doi: 10.1175/
 596 JPO2934.1
- 597 Hogg, A. M., Meredith, M. P., Chambers, D. P., Abrahamsen, E. P., Hughes,
 598 C. W., & Morrison, A. K. (2015). Recent trends in the Southern Ocean
 599 eddy field. *Journal of Geophysical Research: Oceans*, 120(1), 257-267. doi:
 600 10.1002/2014JC010470
- 601 Hu, S., Sprintall, J., Guan, C., McPhaden, M. J., Wang, F., Hu, D., & Cai,
 602 W. (2020, 2). Deep-reaching acceleration of global mean ocean circula-
 603 tion over the past two decades. *Science Advances*, 6(6), eaax7727. doi:
 604 10.1126/sciadv.aax7727
- 605 Japan Meteorological Agency, Japan. (2013). *Jra-55: Japanese 55-year reanalysis,*
 606 *daily 3-hourly and 6-hourly data.* Boulder CO: Research Data Archive at the Na-
 607 tional Center for Atmospheric Research, Computational and Information Systems
 608 Laboratory. Retrieved from <https://doi.org/10.5065/D6HH6H41>
- 609 Kang, D., & Curchitser, E. N. (2013). Gulf stream eddy characteristics in a high-
 610 resolution ocean model. *Journal of Geophysical Research: Oceans*, 118(9), 4474-
 611 4487. Retrieved from <https://agupubs.onlinelibrary.wiley.com/doi/abs/10.1002/jgrc.20318> doi: <https://doi.org/10.1002/jgrc.20318>
- 612 Kang, D., & Curchitser, E. N. (2017). On the Evaluation of Seasonal Variability of
 613 the Ocean Kinetic Energy. *Geophysical Research Letters*, 47, 1675-1583. doi: 10
 614 .1175/JPO-D-17-0063.1
- 615 Li, G., Cheng, L., Zhu, J., Trenberth, K. E., Mann, M. E., & Abraham, J. P. (2020).
 616 Increasing ocean stratification over the past half-century. *Nature Climate Change*,
 617 1-8. doi: 10.1038/s41558-020-00918-2
- 618 Martínez-Moreno, J., Hogg, A. M., England, M., Constantinou, N. C., Kiss, A. E.,
 619 & Morrison, A. K. (2021). Global changes in oceanic mesoscale currents over the
 620 satellite altimetry record. *Journal of Advances in Modeling Earth Systems*, 0(ja).
 621 doi: 10.1029/2019MS001769
- 622 Martínez-Moreno, J., Hogg, A. M., Kiss, A. E., Constantinou, N. C., & Morrison,

- 624 A. K. (2019). Kinetic energy of eddy-like features from sea surface altimetry. *Journal of Advances in Modeling Earth Systems*, 11(10), 3090-3105. doi: 10.1029/2019MS001769
- 625
- 626
- 627 Patel, R. S., Llort, J., Strutton, P. G., Phillips, H. E., Moreau, S., Pardo, P. C., & Lenton, A. (2020). The Biogeochemical Structure of Southern Ocean Mesoscale Eddies. *Journal of Geophysical Research: Oceans*, 125(8). doi: 10.1029/2020jc016115
- 628
- 629
- 630
- 631 Pilo, G. S., Mata, M. M., & Azevedo, J. L. L. (2015). Eddy surface properties and propagation at Southern Hemisphere western boundary current systems. *Ocean Science*, 11(4), 629–641. doi: 10.5194/os-11-629-2015
- 632
- 633
- 634 Qiu, B. (1999). Seasonal Eddy Field Modulation of the North Pacific Subtropical Counter-current: TOPEX/Poseidon Observations and Theory. *Journal of Physical Oceanography*, 29(10), 2471–2486. doi: 10.1175/1520-0485(1999)029<2471:sefmot>2.0.co;2
- 635
- 636
- 637
- 638 Qiu, B., & Chen, S. (2004). Seasonal Modulations in the Eddy Field of the South Pacific Ocean. *Journal of Physical Oceanography*, 34(7), 1515–1527. doi: 10.1175/1520-0485(2004)034<1515:smitef>2.0.co;2
- 639
- 640
- 641 Qiu, B., Chen, S., Klein, P., Sasaki, H., & Sasai, Y. (2014). Seasonal Mesoscale and Submesoscale Eddy Variability along the North Pacific Subtropical Counter-current. *Journal of Physical Oceanography*, 44(12), 3079–3098. doi: 10.1175/JPO-D-14-0071.1
- 642
- 643
- 644
- 645 Ruela, R., Sousa, M. C., deCastro, M., & Dias, J. M. (2020). Global and regional evolution of sea surface temperature under climate change. *Global and Planetary Change*, 190, 103190. doi: 10.1016/j.gloplacha.2020.103190
- 646
- 647
- 648 Sasaki, H., Klein, P., Qiu, B., & Sasai, Y. (2014). Impact of oceanic-scale interactions on the seasonal modulation of ocean dynamics by the atmosphere. *Nature Communications*, 5(1), 5636. doi: 10.1038/ncomms6636
- 649
- 650
- 651 Schubert, R., Schwarzkopf, F. U., Baschek, B., & Biastoch, A. (2019). Submesoscale Impacts on Mesoscale Agulhas Dynamics. *Journal of Advances in Modeling Earth Systems*, 11(8), 2745–2767. doi: 10.1029/2019ms001724
- 652
- 653
- 654 Siegel, D., Peterson, P., DJ, M., Maritorena, S., & Nelson, N. (2011). Bio-optical footprints created by mesoscale eddies in the Sargasso Sea. *Geophysical Research Letters*, 38(13), n/a-n/a. doi: 10.1029/2011GL047660
- 655
- 656

- 657 Uchida, T., Abernathey, R., & Smith, S. (2017). Seasonality of eddy kinetic energy
658 in an eddy permitting global climate model. *Ocean Modelling*, 118, 41–58. doi: 10
659 .1016/j.ocemod.2017.08.006
- 660 Wunsch, C. (2020). Is The Ocean Speeding Up? Ocean Surface Energy Trends.
661 *Journal of Physical Oceanography*, 50(11), 1–45. doi: 10.1175/jpo-d-20-0082.1
- 662 Wunsch, C., & Ferrari, R. (2004). Vertical mixing, energy, and the general circulation
663 of the oceans. *Annual Review of Fluid Mechanics*, 36(1), 281–314. doi: 10
664 .1146/annurev.fluid.36.050802.122121
- 665 Wyrtki, K., Magaard, L., & Hager, J. (1976). Eddy energy in the oceans. *Journal of
666 Geophysical Research*, 81(15), 2641–2646. doi: 10.1029/JC081i015p02641
- 667 Yue, S., & Wang, C. (2004). The Mann-Kendall Test Modified by Effective Sample
668 Size to Detect Trend in Serially Correlated Hydrological Series. *Water Resources
669 Management*, 18(3), 201–218. doi: 10.1023/b:warm.0000043140.61082.60
- 670 Zamudio, L., Hurlbert, H. E., Metzger, E. J., Morey, S. L., O'Brien, J. J., Tilburg,
671 C., & Zavala-Hidalgo, J. (2006). Interannual variability of Tehuantepec ed-
672 dies. *Journal of Geophysical Research: Oceans (1978–2012)*, 111(C5). doi:
673 10.1029/2005JC003182